Available online at www.sciencedirect.com

SCIENCE DIRECT®

Cement and Concrete Research 36 (2006) 171 – 188

Cement and Concrete Research

Deterministic size effect in the strength of cracked concrete structures

B.L. Karihaloo*, H.M. Abdalla, Q.Z. Xiao

School of Engineering, Cardiff University, Queen's Buildings, P.O. Box 925, Cardiff, CF24 0YF, UK

Received 18 March 2005; accepted 20 April 2005

Abstract

This paper is concerned with identifying and quantifying the deterministic (as opposed to statistical) size effect in the strength of cracked concrete structures that is believed to be a result of stress discontinuities introduced by the cracks. For this, the strength of geometrically similar pre-cracked specimens of varying sizes made from three concrete mixes is measured in three-point bend and wedge splitting geometries. The true, size-independent specific fracture energy and the corresponding tension softening diagram of each of the three mixes are independently established in order to exclude their influence on the strength size effect. The test results show that the deterministic strength size effect weakens as the size of the crack reduces. This is confirmed by theoretical/computational studies based on the fictitious crack model in the range of sizes tested in the laboratory. The theoretical/computational model has been extended beyond this limited range to include cracked concrete structures in the size range 1 : 80. The computational results have been fitted by a simple strength size effect formula with appropriate asymptotic behaviour at both size extremes. The three unknown coefficients in this formula depend only on the size of the crack and they can be obtained by conducting tests on geometrically similar specimens of any shape but of varying sizes that can be conveniently handled in a laboratory. The three material properties of the concrete mix appearing in this formula, namely the Young modulus E, the direct tensile strength f_t and the size-independent specific fracture energy G_F must be independently measured.

Keywords: Concrete; Fracture toughness; Modeling; Size effect; Tensile properties

1. Introduction

Leicester [1,2] seems to have been the first to identify two fundamental causes of size effect in structures made from quasi-brittle materials, such as concrete, namely the material heterogeneity and the occurrence of discontinuities in the flow of stress, such as at cracks and notches. In the latter case he proposed the following size effect formula

$$(\sigma_N)_u = A_1/W^s; \qquad s < {}^1/_2. \tag{1}$$

Here, A_1 is a constant, $(\sigma_N)_u$ is the nominal stress at failure of a structure of specified shape and loading condition, and W is a characteristic size of the structure.

In quasi-brittle materials, any crack or notch tips are blunted by the formation of a process zone ahead of them. In this process zone the stresses are redistributed and energy dissipated which is thus not available for crack propagation. The size of this fracture process zone (FPZ) can be commensurate with that of most structural elements. Only in very large structures can this size be regarded as small in comparison with the characteristic dimensions.

The redistribution of stresses and dissipation of energy in the FPZ was not accounted for in the derivation of (1). That was done by Bazant [3] who derived the following formula for geometrically similar structures

$$(\sigma_N)_u = \frac{A_2}{(1 + W/B_2)^{\frac{1}{2}}}, \tag{2}$$

where A_2 and B_2 are positive coefficients. Formula (2) also reduces to the linear elastic fracture mechanics as $W \to \infty$ when the size of the FPZ is very small in comparison with W. In fact formula (2) can be established by Taylor's expansion from this asymptotic limit (Karihaloo [4]). Since its appearance in the literature in 1984, formula (2) has been rederived from energy considerations and asymptotic

* Corresponding author. Tel.: +44 29 20874934; fax: +44 29 20874597.
E-mail address: karihaloob@cardiff.ac.uk (B.L. Karihaloo).

0008-8846/$ - see front matter © 2005 Elsevier Ltd. All rights reserved.
doi:10.1016/j.cemconres.2005.04.007

matching techniques (see, e.g. Bazant [5]; Bazant and Chen [6]). The positive coefficients A_2 and B_2 are related to the specific fracture energy G_f and the FPZ size c_f measured on a very large specimen (W?8 with $a/W\to\infty$ fixed), as well as the non-dimensional geometry factor $g(\alpha)$ and its first derivative $g'(\alpha)$. The geometry factor $g(\alpha)$ depends on the notch to depth ratio $\alpha=a/W$ and is different for different test specimen shapes

$$A_2=\left(\frac{EG_f}{g'(\alpha)c_f}\right)^{\frac{1}{2}};\qquad B_2=c_f\frac{g'(\alpha)}{g(\alpha)}. \tag{3}$$

It has been argued that the relationships between the coefficients A_2 and B_2 and the material properties G_f and c_f (3) can be exploited to determine the latter from tests on notched specimens of various sizes with two-dimensional similarity. For example, tests can be conducted on notched three-point bend (TPB) beams with a fixed α and span to depth ratio for several depth values. The coefficients A_2 and B_2 are determined by a linear regression analysis, after rewriting (2) in the standard form $Y=AX+B$, where $Y=1/(\sigma_N)_u^2$, $X=W$, $A=1/(B_2A_2^2)$ and $B=1/A_2^2$.

Another approach to capturing the FPZ within a nonlinear theory of fracture for quasi-brittle materials is the so-called fictitious crack model (FCM) of Hillerborg et al. [7]. In this model, the FPZ ahead of a real crack is replaced with a fictitious crack in which the material exhibits softening with a residual stress transfer capability across the crack faces dependent on the crack opening displacement (COD), $\sigma(w)$. The faces of the fictitious crack are assumed to close smoothly near the tips so that the stress is finite at the fictitious crack tip and equal to the tensile strength f_t of the quasi-brittle material. Thus the net stress intensity factor (SIF) (i.e. the SIF due to external loading less the factor due to the closure pressure in the FPZ) vanishes at the fictitious crack tip.

This approach was adopted by Karihaloo [8] who arrived at the formula

$$(\sigma_N)_u=A_3\left(1-\frac{B_3}{W}\right)^{\frac{1}{2}}, \tag{4}$$

where

$$A_3=(\sigma_N)_{u\infty};\quad B_3=\frac{1}{2}l_{p\infty}\frac{g'(\alpha)}{g(\alpha)}. \tag{5}$$

Here, $l_{p\infty}$ and $(\sigma_N)_{u\infty}$ refer to the size of the FPZ in a very large specimen ($W\to\infty$) and its nominal strength. It was argued by Karihaloo [8] that $l_{p\infty}$ and $(\sigma_N)_{u\infty}$ can be obtained by considering only the singular term of the stress field ahead of a pre-existing crack, whereas for normal size structures higher order terms need to be considered to take into account the relatively large size of the FPZ in the FCM.

In the derivation of formula (4) several approximations and assumptions were made, as a result of which its predictions for small values of W were suspect. This was pointed out by Planas et al. [9] and by Karihaloo et al. [10]. The latter authors also made a tentative attempt at dispensing with some of the approximations and assumptions in its derivation. Apart from these drawbacks, it is not clear how the asymptotic properties G_f and $l_{p\infty}$ can be used for the analysis of real structures. Moreover, it transpires that both G_f and $l_{p\infty}$ (or c_f in formula (2)) cannot be regarded as material properties because they vary with α, W and the shape of the test specimen. That brings us to the essential question that we shall attempt to answer in this paper. How much of the size effect in the strength of a quasi-brittle structure predicted by formula (4) (or formula (2)) is a result of the intrinsic size effect in the G_f itself? In other words, if the specific fracture energy of a quasi-brittle material that did not depend on the shape and size of the test specimen could be independently determined, would a structure made of such a material still exhibit a strong size effect in strength?

In this paper we shall revisit the formulation of formula (4) with a view to predicting the observed nominal strengths of notched TPB and wedge splitting (WS) specimens made from normal and high strength concretes (NSC and HSC). Both these specimen geometries belong to the so-called type 2 geometry, i.e. $g(\alpha)>0$, $g'(\alpha)>0$ (Bazant [11]). The paper is organised as follows. In Section 2, the results of a test programme using TPB and WS specimens made of NSC and HSC are summarised with a view to determining the specific fracture energy and the tension softening diagram of the respective concrete mix that are independent of the specimen size and shape. The latter are then used in Section 3 to predict the nominal strength of the test specimens using the FCM of Hillerborg et al. [7]. Section 4 is devoted to a comparison of the test results with the theoretical predictions and with the prediction of formula (2). Finally, in Section 5 we discuss the findings and provide an answer to the fundamental question posed above, and in Section 6 we propose an improved formula for predicting the strength size effect over a large size range of 1:80. The major conclusions are summarised in Section 7.

2. Test results, G_F and $\sigma(w)$

Tests were conducted on notched TPB and WS specimens (for full details, see Abdalla and Karihaloo [12]). Notched beams of different depths W (100, 200, 300 and 400 mm) with a constant span to depth ratio of 4 were tested in three point bending (Fig. 1). The notch to depth ratios a/W were selected to be 0.05, 0.10, 0.30 and 0.50. The notch was introduced with a diamond saw. Four beams were tested for each notch to depth ratio and each depth. Ready mix NSC (with an average compressive strength f_c of 55 MPa) was used in view of the large volume of concrete needed. The testing was carried out using a Dartec closed-loop testing machine controlled by the signal from a clip gauge measuring the crack mouth opening displacement (CMOD)

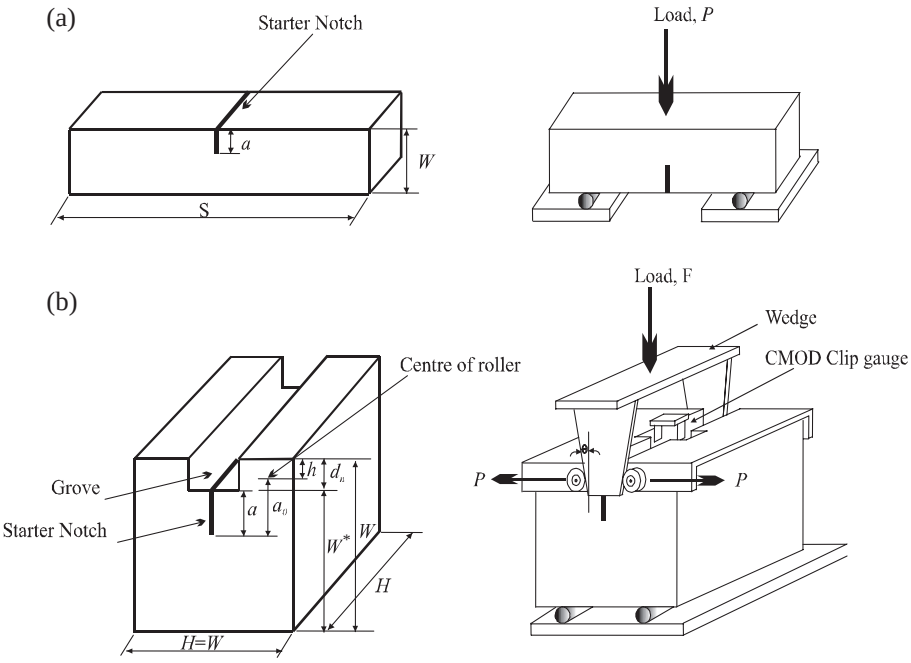

Fig. 1. Geometry and loading arrangements: (a) TPB specimen; (b) WS specimen.

and placed between knife edges at the mouth of the starter notch.

WS tests were carried out on NSC and HSC. These concretes were mixed in the laboratory since only small amounts were needed. Their average compressive strengths were 60 and 100 MPa, respectively. Ninety-six specimens of different sizes W (100, 200 and 300 mm) were tested (Fig. 1). The notch to depth ratios $a_0/(W-h)$ were selected to be 0.20, 0.30, 0.40 and 0.50 (the corresponding a/W^* ratios are 0.16, 0.26, 0.36 and 0.46, see Fig. 1). The distance h is given in Table 3. The testing was carried out using a Dartic closed-loop testing machine controlled by the signal from the CMOD gauge at a rate of 0.0002 mm/s. The loading arrangements are shown in Fig. 1.

Typical recorded load-displacement (TPB) and load-CMOD (WS) diagrams are shown in Fig. 2 from which the specific fracture energy was calculated using

$$G_f(\alpha, W) = \frac{1}{(W-a)B}\int P d\delta \quad \text{(TPB)} \tag{6}$$

$$= \frac{1}{(W^*-a)H}\int \frac{F}{2\tan\theta} d(\text{CMOD}) \quad \text{(WS)}$$

where B is the thickness of beam.

The value of the specific fracture energy so determined varies with the size and the notch to depth ratio α. This value is therefore designated $G_f(\alpha, W)$. It decreases with increasing α but increases with increasing W (for details, see Abdalla and Karihaloo [12]).

Hu and Wittmann [13,14] had addressed the possibility that the fracture energy required to create a crack is influenced by the size of the FPZ which in turn is influenced by the free boundary of the test specimen. To consider the boundary effect on the local fracture energy distribution in the FPZ, they assumed a bilinear energy distribution in the ligament ahead of the pre-existing crack. The bilinear approximation consists of a horizontal line with the value

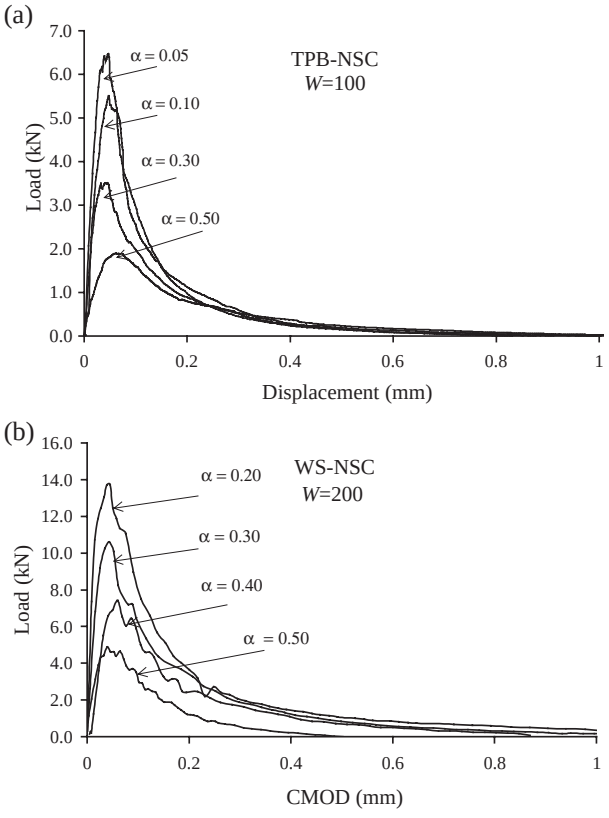

Fig. 2. Typical load-displacement diagrams in TPB test (a) and load-CMOD diagrams in WS test (b).

G_F and a descending branch that reduces to zero at the back face of the specimen. The intersection of these two lines defines the transition ligament size a_1 (Hu and Wittmann [14]) which depends on both the material properties and specimen geometry. In general the ligament size $(W-a)$ (or W^*-a in WS geometry) is always larger than the transition ligament size a_1, so that

$$G_f(\alpha, W) = G_F\left\{1 - \frac{1}{2}\frac{a_1/W}{(1-\alpha)}\right\} \tag{7}$$

As the number of measured $G_f(\alpha, W)$ for each size W and each notch to depth ratio α exceeds the number of unknowns in (7) which is only 2, namely G_F and a_1, the over-determined system of equations is solved by a least squares method to get the best estimate of G_F and a_1.

The boundary effect concept was further developed by Duan et al. [15] based on the TPB test results of Nallathambi et al. [16,17] and confirmed by independent tests on TPB and WS specimens described above by Abdalla and Karihaloo [12]. It should be mentioned that the boundary effect concept is similar in principle to the perturbed ligament model of Planas and Elices [18], but it is much simpler to implement in practice.

The application of the boundary effect concept to the test results $G_f(\alpha, W)$ indeed gives a specific fracture energy value G_F that is independent of the size (α, W) and shape of the test specimen. This may be judged by the values reported in Table 1.

For both the TPB and WS specimens the size-independent specific fracture energy G_F (Table 1) was estimated from three or four sizes with four notch to depth ratios. However, Abdalla and Karihaloo [12] also observed that the same value of G_F for a concrete mix could also be obtained by testing specimens of a single size, one half of them containing a very shallow starter crack ($\alpha \leq 0.10$ for TPB and $\alpha \leq 0.16$ for WS) and the other half a deep starter crack ($\alpha \geq 0.50$ for TPB and WS). This observation was confirmed recently (Karihaloo et al. [19]) by re-evaluation of a large body of test data on measured $G_f(\alpha, W)$ of concrete mixes available in the literature. This conformation paved a way for a simple and practical means of determining G_F of concrete. They also provided guidance for the selection of the specimen dimensions based on the maximum size of aggregate in the concrete mix.

In the context of the FCM (Hillerborg et al. [7]) the true specific fracture energy obtained above is exactly equal to

Table 1
Size-independent specific fracture energy G_F

TPB specimens of NSC (55 MPa)	W mm	100	200	300	400
	G_F N/m	140	144	137	143
	a_l mm	54	104	117	149
WS specimens	W mm	100	200	300	
NSC (60 MPa)	G_F N/m	153	155	156	
	a_l mm	79	136	166	
HSC (100 MPa)	G_F N/m	125	122	123	
	a_l mm	74	128	187	

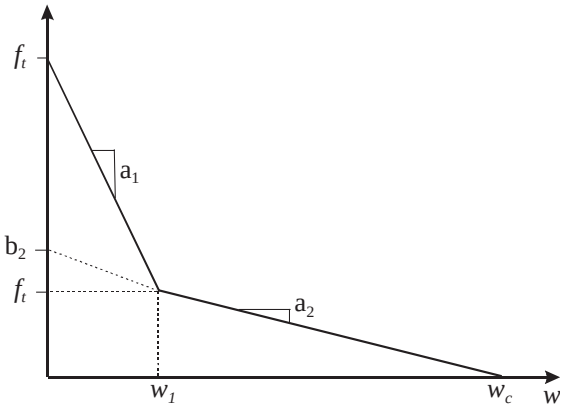

Fig. 3. Bilinear tension softening diagram $\sigma(w)$.

the area under the cohesive stress-separation diagram $\sigma(w)$ (i.e. the tension softening diagram) in the fictitious crack (i.e. the FPZ)

$$G_F = \int_0^{w_c} \sigma(w)dw, \tag{8}$$

where w_c is the critical opening of the real crack tip when it begins to grow.

As the tension softening region is generally discontinuous, a direct determination of $\sigma(w)$ is an impossible task. It is therefore often determined using an inverse identification procedure. Many such procedures have been proposed (Roelfstra and Wittmann [20]; Ulfkjaer et al. [21]; Olesen [22]; Bolzon et al. [23]). In each of these procedures, the shape of the tension softening diagram is assumed a priori and the parameters describing it identified in such a way that the global load-deformation response of the test specimen is reproduced with a desired degree of accuracy. By far the most popular approximation of the $\sigma(w)$ diagram is the bilinear one shown in Fig. 3, so that (8) reduces to

$$G_F = \frac{1}{2}(f_t w_1 + f_1 w_c), \tag{9}$$

where w_1, f_1 and w_c are to be identified. In this work, the simple inverse identification procedure of Olesen [22] based on a nonlinear hinge model for the real and fictitious crack was used to identify these three parameters for the three concrete mixes tested using the TPB and WS specimens. The global load-CMOD response of the specimens was reproduced for all W and α and the procedure described in Abdalla and Karihaloo [24] was used to determine the parameters w_1, f_1 and w_c corresponding to the size-independent G_F of concrete mixes (Table 1). The resulting parameters of the bilinear $\sigma(w)$ diagram for the three mixes are given in Table 2.

3. Theoretical predictions

In the derivation of formula (4) (Karihaloo [8]) it was recognised that quasi-brittle materials develop a diffuse FPZ before the formation of a traction-free crack whose size can

Table 2
Elastic properties and parameters of $\sigma(w)$ diagram for the three test concrete mixes

Mix	f_c (MPa)	f_t (MPa)	G_F (N/m)	E (GPa)	w_1 (mm)	f_1 (MPa)	w_c (mm)	$l_{ch}=EG_F/f_t^2$ (mm)
NSC for TPB	55	2.67	141	36.9	0.049	0.457	0.333	729.8
NSC for WS	60	2.80	155	38.3	0.051	0.524	0.318	757.2
HSC for WS	100	4.00	123	43.0	0.017	1.36	0.132	330.6

The direct tensile strength was assumed to be $f_t=0.65\,f_{st}$, where f_{st} is the indirect tensile strength, namely the split cylinder strength (Neville [37]).

be commensurate with that of a small test specimen. Within this zone the stresses are redistributed so that it is necessary to consider not only the singular term in the asymptotic crack tip field but also higher order, non-singular terms. In the derivation, Karihaloo [8] used approximations for the higher order terms, as well as the weight (Green's) functions for a semi-infinite crack in an infinite plane instead of a finite size crack in a finite TPB or WS specimen. These approximations have now been eliminated by taking into account accurate higher order terms of the crack tip asymptotic field, as well as by using accurate weight functions for a finite crack. Some preliminary results have been previously reported (Karihaloo et al. [10]).

In common with the earlier derivation (Karihaloo [8]), the traction-free crack with a FPZ of length l_p at its tip is decomposed into a traction-free crack (Fig. 4) with the following stress field at its tip

$$\sigma_y(r)\equiv\sigma_0(r)=\frac{a_1}{\sqrt{r}}+3a_3\sqrt{r}+5a_5r^{\frac{3}{2}} \tag{10}$$

and the FPZ with the stress $|\sigma(s)-\sigma(l_p-s)|$ and the displacement $w(s)$ across its faces. In (10), a_1 is related to the mode I SIF K_I via $a_1=K_I/\sqrt{2\pi}$. The dimensioned coefficients a_1, a_3 and a_5 depend on the crack length, applied load σ and size and geometry of the body.

For a TPB with a span to depth ratio β of 4 considered in the current study, the coefficients a_1, a_3, a_5 are (Karihaloo and Xiao [25])

$$\begin{aligned}
a_1&=\sigma\sqrt{W}k_4(\alpha)\\
a_3&=\frac{\sigma}{\sqrt{W}}g_4^3(\alpha)\\
a_5&=\frac{\sigma}{W^{3/2}}g_4^5(\alpha)
\end{aligned}\tag{11}$$

where

$$\begin{aligned}
k_4(\alpha)&=\frac{\sqrt{\alpha}p_4(\alpha)}{\sqrt{2\pi}(1-\alpha)^{3/2}(1+3\alpha)}\\
p_4(\alpha)&=1.9+0.41\alpha+0.51\alpha^2-0.17\alpha^3\\
g_4^3(\alpha)&=-148.73\alpha^5+233.48\alpha^4-153.97\alpha^3+49.515\alpha^2\\
&\quad-9.2406\alpha+0.6534\\
g_4^5(\alpha)&=2765.2\alpha^6-5869.4\alpha^5+4919.3\alpha^4-2084.4\alpha^3\\
&\quad+468.48\alpha^2-52.998\alpha+2.1491
\end{aligned}\tag{12}$$

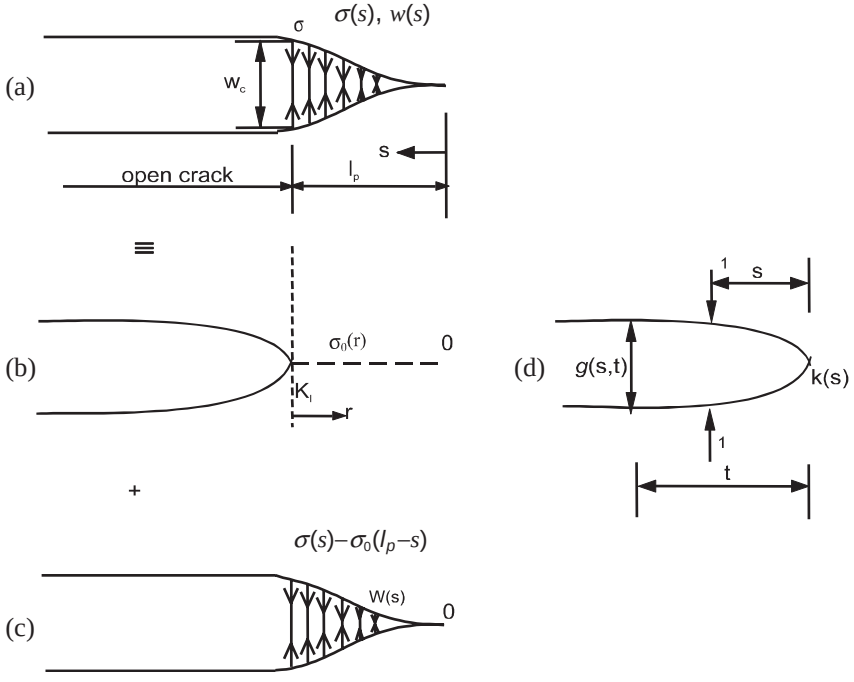

Fig. 4. Decomposition of a traction free crack with a FPZ of length l_p (a) into the traction free crack with stress $\sigma_0(r)$ ahead of crack tip (b) and the FPZ with stress $[\sigma(s)-\sigma_0(l_p-s)]$ and COD $w(s)$ (c). As the faces close smoothly the SIF at 0 will vanish. $k(s)$ is the SIF due to unit concentrated loads at s, $g(s, t)$ is the corresponding COD at location t (d) (From Karihaloo [4]).

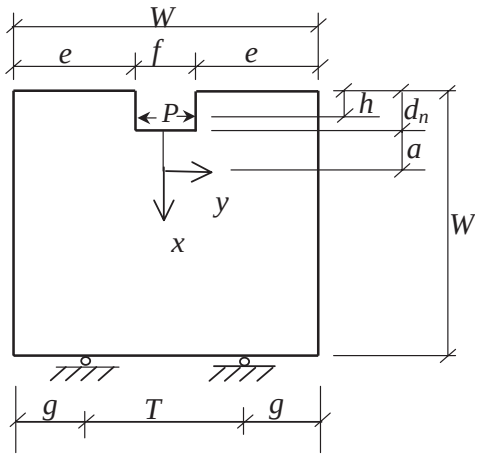

Fig. 5. WS geometry.

and $\sigma = 6P/W$ and the subscript 4 refers to the span to depth ratio $\beta = 4$. P is the applied point load per unit thickness (m). The dimensions of σ and W are MPa and m, respectively.

For the WS geometry shown in Fig. 5, the coefficients a_1, a_3, a_5 are normalized as

$$k(\alpha) = \frac{K_I}{\sigma\sqrt{2\pi W}} = \frac{a_1}{\sigma\sqrt{W}}$$

$$g_3(\alpha) = \frac{a_3}{\sigma/\sqrt{W}} = \frac{a_3}{\sigma}\sqrt{W}$$

$$g_5(\alpha) = \frac{a_5}{\sigma/W^{3/2}} = \frac{a_5}{\sigma}W^{3/2} \tag{13}$$

where $\sigma = P/W$ for the concentrated loading arrangement shown in Fig. 5. P is the point load per unit thickness (mm). The dimensions of σ and W are MPa and mm, respectively. For the sizes listed in Table 3 and considered in this study, the dimensionless functions are fitted from numerical results with error <0.1% as (Karihaloo et al. [26])

$$k(\alpha) = 508.9\alpha^5 - 841.5\alpha^4 + 540.7\alpha^3 - 155.1\alpha^2 + 23.96\alpha + 0.4557$$

$$g_3(\alpha) = -7724\alpha^6 + 14959\alpha^5 - 10977\alpha^4 + 3587\alpha^3 - 434.6\alpha^2 - 25.24\alpha + 4.1$$

$$g_5(\alpha) = -18785\alpha^6 + 36373\alpha^5 - 26375\alpha^4 + 8695.2\alpha^3 - 1331.7\alpha^2 + 128.1\alpha - 13.79 \tag{14}$$

for $W = 100$ mm, and

$$k(\alpha) = 342.3\alpha^5 - 527.8\alpha^4 + 331.4\alpha^3 - 96.5\alpha^2 + 17.39\alpha + 0.6531$$

$$g_3(\alpha) = -4945\alpha^6 + 8966\alpha^5 - 6054\alpha^4 + 1658.5\alpha^3 - 59.3\alpha^2 - 59.44\alpha + 5.17$$

$$g_5(\alpha) = 1117.7\alpha^6 - 13095\alpha^5 + 21537\alpha^4 - 13975\alpha^3 - 4023.7\alpha^2 - 436.3\alpha + 4.76 \tag{15}$$

for $W = 200$ mm, and

$$k(\alpha) = 552.9\alpha^5 - 946.7\alpha^4 + 630.2\alpha^3 - 189.4\alpha^2 + 29.47\alpha + 0.1645$$

$$g_3(\alpha) = -7144\alpha^6 + 13534\alpha^5 - 9444\alpha^4 + 2704.5\alpha^3 - 158.2\alpha^2 - 67.26\alpha + 6.25$$

$$g_5(\alpha) = -2652\alpha^6 - 5166\alpha^5 + 15504\alpha^4 - 12020\alpha^3 + 3814\alpha^2 - 449.69\alpha + 7.24 \tag{16}$$

for $W = 300$ mm.

The opening displacement of the cohesive crack faces $w(t)$ (representing the FPZ) can be expressed as the solution of the following singular integral equation (see Fig. 4)

$$\int_0^{l_p} g(s,t;a)\left[\sigma(s) - \sigma_0\left(l_p - s\right)\right]ds = -w(t). \tag{17}$$

The finite tensile strength of concrete requires that SIF vanish at the FPZ tip. This in turn requires that the faces of FPZ close smoothly, i.e.

$$\int_0^{l_p} k(s;a)\left[\sigma(s) - \sigma_0\left(l_p - s\right)\right]ds = 0. \tag{18}$$

Of course, it is not always necessary to impose the condition that the SIF vanishes at the FPZ tip (see, e.g., Elices et al. [27]). In NSC, the FPZ is often surrounded by a zone of microcracks (corresponding to the pre-peak nonlinearity), so that the SIF is finite at the FPZ tip. However, this has been shown to have a negligible effect on the results (Alaee and Karihaloo [28]).

The weight functions $g(s, t; a)$ and $k(s; a)$ are the respective COD at the location t and the SIF at the crack tip of a single edge cracked specimen of finite size due to a pair of unit normal forces at s on the crack faces (Fig. 4d). Both $k(s; a)$ and $g(s, t; a)$ have been derived by Xiao and Karihaloo [29].

Table 3
WS specimen dimensions (mm)

Specimen Size	100	200	300
Width W	100	200	300
Thickness B	100	200	300
a	4~64	8.5~136	12.65~202.4
d_n	20	30	47
h	15	25	35
e	35	70	105
f	30	60	90
g	25	50	75
T	50	100	150

In this study, we have further enhanced the accuracy of $k(s; a)$ with the use of the hybrid crack element (Karihaloo and Xiao [30]), and the result is

$$k(s;a) = \sqrt{\frac{2}{\pi s}} + A_1\sqrt{2\pi} \tag{19}$$

A_1 depends on the size and geometry of the body W, and the size of the crack a

$$A_1(\alpha,\gamma) = \left(W_0/W^*\right)^{\frac{1}{2}} \sum_{j=0}^{5} f_{1j}(\alpha)\gamma^j \tag{20}$$

where $\alpha = a/W^*$, $\gamma = s/a$ and a is the crack length. W_0 represents a characteristic size of the specimen used for the calculation of the weight functions below, W^* represents the actual size of the specimen for which the weight function is used.

For the geometry shown in Fig. 6, which may be used for the TPB in which case $W = W^*$ in m, the non-dimensional functions $f_{1j}(\alpha)$ are

$$f_{10}(\alpha) = 11.026\alpha^5 - 13.823\alpha^4 + 4.0226\alpha^3 + 2.0164\alpha^2 - 0.5575\alpha + 0.0963$$

$$f_{11}(\alpha) = 429.38\alpha^5 - 738.19\alpha^4 + 500.78\alpha^3 - 149.56\alpha^2 + 23.384\alpha + 0.8838$$

$$f_{12}(\alpha) = 40.96\alpha^2 - 75.609\alpha + 22.899, \quad \alpha > 0.6$$

$$f_{13}(\alpha) = -92.65\alpha^2 + 157.76\alpha + 50.355, \quad \alpha > 0.6$$

$$f_{14}(\alpha) = 91.795\alpha^2 - 149.99\alpha + 48.896, \quad \alpha > 0.6$$

$$f_{15}(\alpha) = -33.055\alpha^2 + 52.752\alpha - 17.394, \quad \alpha > 0.6$$

$$f_{12}(\alpha) = -13.775\alpha^3 + 5.095\alpha^2 - 4.458\alpha - 3.9128, \quad \alpha \le 0.6$$

$$f_{13}(\alpha) = 19.993\alpha^2 - 6.4559\alpha + 7.6043, \quad \alpha \le 0.6$$

$$f_{14}(\alpha) = -18.031\alpha^2 + 7.7761\alpha - 6.2402, \quad \alpha \le 0.6$$

$$f_{15}(\alpha) = -4.6046\alpha^3 + 10.596\alpha^2 - 4.0866\alpha + 1.9845, \quad \alpha \le 0.6 \tag{21}$$

with $W_0 = 1$ m.

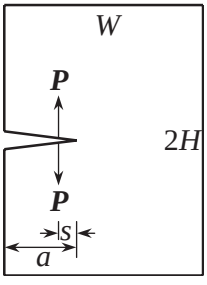

Fig. 6. A single edge cracked plate subjected to a pair of wedge forces $P = 1$.

For the WS geometry (Fig. 5), $W^* = W - d_n$ in mm we have also fitted the numerical results for $W = 100$ mm, $d_n = 20$ mm, $f = 30$ mm, and $e = 35$ mm as

$$f_{10}(\alpha) = -10.837\alpha^5 + 28.701\alpha^4 - 29.259\alpha^3 + 15.251\alpha^2 - 4.3207\alpha + 0.8133$$

$$f_{11}(\alpha) = 123.31\alpha^5 - 258.91\alpha^4 + 214.08\alpha^3 - 90.404\alpha^2 + 22.249\alpha - 3.4214$$

$$f_{12}(\alpha) = -218.06\alpha^5 + 516.02\alpha^4 - 457.94\alpha^3 + 209.05\alpha^2 - 55.104\alpha + 9.3255$$

$$f_{13}(\alpha) = 393\alpha^5 - 915.81\alpha^4 + 784.8\alpha^3 - 341.39\alpha^2 + 85.598\alpha - 14.05$$

$$f_{14}(\alpha) = -349.29\alpha^5 + 805.58\alpha^4 - 674.31\alpha^3 + 282.61\alpha^2 - 67.783\alpha + 10.738$$

$$f_{15}(\alpha) = 118.92\alpha^5 - 272.5\alpha^4 + 224.77\alpha^3 - 91.783\alpha^2 + 21.249\alpha - 3.2529 \tag{22}$$

Here, $W_0 = 85$ mm. The above results can also be used for WS specimens with different W^* values.

As the singular integral Eqs. (17) and (18) will be solved numerically, $g(s, t; a)$ can be established directly from $k(s; a)$ with the use of Castigliano's theorem or the so-called Paris equation (Paris [31]; Tada et al. [32]).

$$g(s,t;a) = \frac{2}{E'}\int_{a-\min(s,t)}^{a} k(x-a+s;x)k(x-a+t;x)dx \tag{23}$$

where $E' = E$ for plane stress and $E' = E/(1-\upsilon^2)$ for plane strain and $\min(s, t)$ means the smaller of the distances s and t. Xiao and Karihaloo [29] have shown that the COD so obtained is quite accurate.

In the earlier formulation leading to Eq. (4) (Karihaloo [8]) the following crucial approximations were made: (i) the higher order coefficient a_3 was inferred indirectly and a_5 was not included; (ii) only the first terms in the weight functions (19) and (23) were used. These terms correspond to a semi-infinite crack in an infinite body and not the finite TPB or WS specimens considered; (iii) with these approximations, the system of Eqs. (17) and (18) was solved analytically in an indirect manner. The COD, $w(s)$, in the FPZ $0 \le s \le l_p$ was approximated by a polynomial in s, and $\sigma(s)$ and l_p were solved analytically from (17) and (18) for prescribed σ (i.e. K_I). The distance s was then eliminated from the assumed $w(s)$ and the calculated $\sigma(s)$ to establish the tension softening relationship $\sigma(w)$.

As a result of the above approximations, the $\sigma(w)$ relationship so obtained became dependent on the geometry

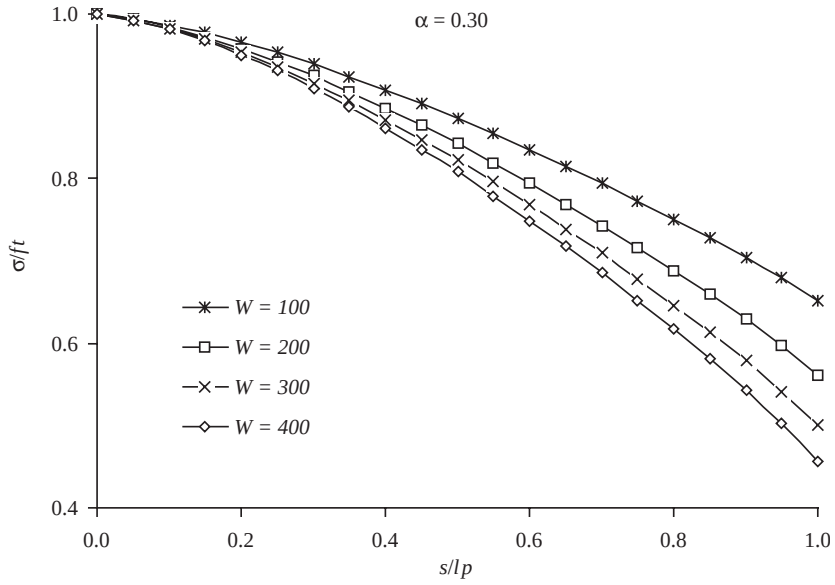

Fig. 7. Distribution of the cohesive stress in the FPZ for TPB specimens with $\alpha = 0.30$ and various W.

of the structure and external loading (i.e. on σ and a_3) and no longer reflected a true material property, as it should. Additionally, the nominal strength formula (4) predicted an arbitrary lower limit on the structural size $W > B_3$ in order for it to have a physical meaning.

The above exact formulation has overcome these drawbacks. However, it is now necessary to prescribe the actual $\sigma(w)$ diagram for the concrete used for making the TPB beams and WS specimens and to solve the singular integral Eqs. (17) and (18) numerically for the prescribed $\sigma(w)$ diagram (Table 2).

To solve the singular integral Eqs. (17) and (18), the FPZ is divided into segments as is usually done in the boundary element analysis. The cohesive stress $\sigma(s)$ is interpolated by its values at the two end points and assumed to vary linearly within each segment. Eq. (17) is discretized at all nodes except the FPZ tip, where the value of cohesive stress equals f_t. From the discretized system of equations, we can solve the unknown cohesive stresses and external applied stress σ (or l_p) for given l_p (or σ) (details are given in the Appendix). If l_p is given, the discretized system of equations is linear, but non-symmetric. l_p is increased by a step size of 0.5 mm and Eqs. (17) and (18) solved incrementally. In order to integrate accurately the integrals with possible endpoint singularities, we have used the IMSL routine DQDAGS to integrate (23), and the routine DQDAG to integrate (17) and (18) on each segment. Both integrators use a globally adaptive scheme to reduce the absolute error, and handle very well even functions that have endpoint singularities. The desired absolute accuracy was set to 0, while the desired relative accuracy

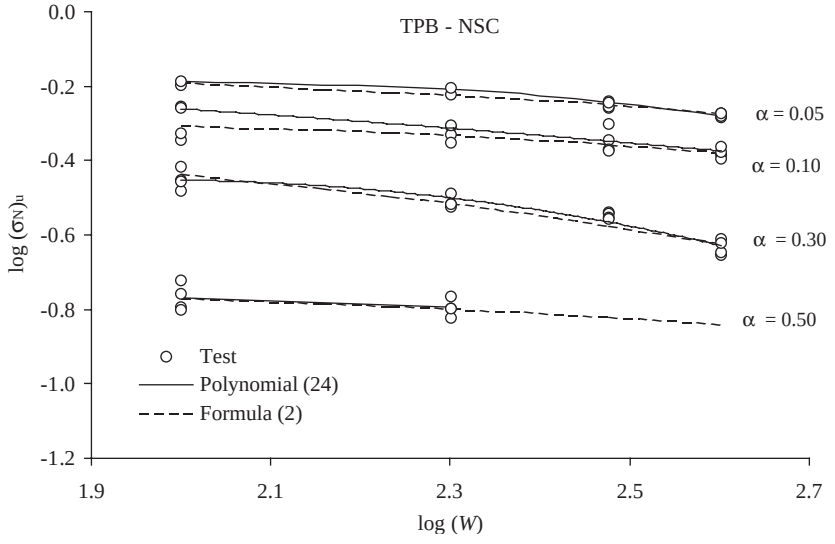

Fig. 8. The variation of the measured nominal strength with the characteristic dimension, W of the TPB specimen compared with polynomial (24) and formula (2).

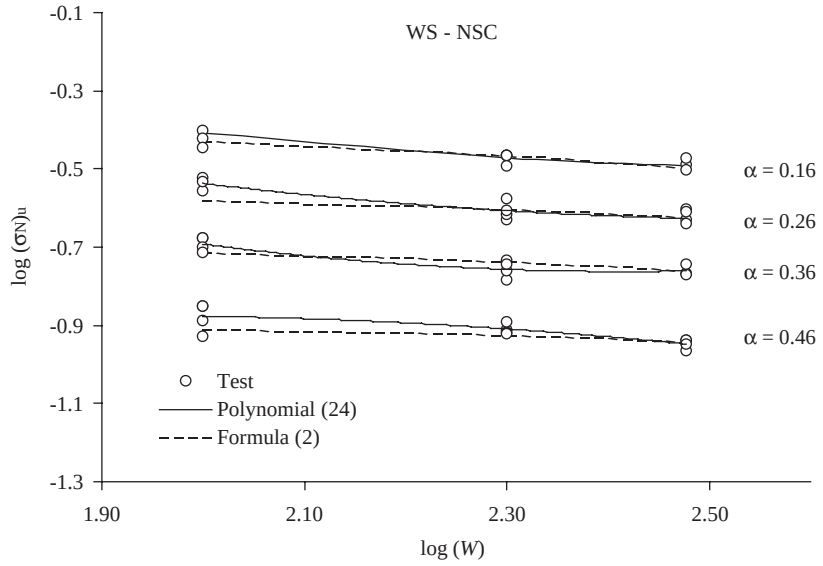

Fig. 9. The variation of the measured nominal strength with the characteristic dimension, W of the WS specimen for NSC compared with polynomial (24) and formula (2).

was set to 10^{-4}. When the FPZ is very small (e.g., l_p is only a few millimetres long), it may be difficult to meet these desired accuracy measures, but such difficulties disappear as the length of FPZ increases. The discretized system of equations at each step is solved by the IMSL high accuracy linear system solver, DLSARG, which solves a general system of linear equations in real variables with iterative refinement. Numerical tests showed that convergent results are obtained with 10–15 divisions of the FPZ. In this study, the FPZ was divided into 20 equal segments.

The typical distribution of the cohesive stress in the FPZ at peak load is shown in Fig. 7, for TPB specimens with $\alpha = 0.30$ and various W values. The distributions are very similar for all values of α, and for all α and W the residual stress level is always above f_1 (Table 2).

4. Comparison of test results with theory and formula (2)

Figs. 8–10 show on a log–log plot the variation of the measured nominal failure strength, $(\sigma_N)_u$, with the characteristic dimension W of the test specimen. The test results are faithfully represented by the following polynomial (coefficient of determination $R^2 \cong 1$)

$$\frac{(\sigma_N)_u}{f_t} = C_1 + C_2\left(\frac{W}{l_{ch}}\right)^2 + C_3\left(\frac{W}{l_{ch}}\right)^3, \quad (24)$$

where the normalising material parameters f_t and l_{ch} of the mixes used in the test specimens are given in Table 2. The coefficients C_1, C_2 and C_3 are given in Table 4. They depend on the notch to depth ratio α. The regression

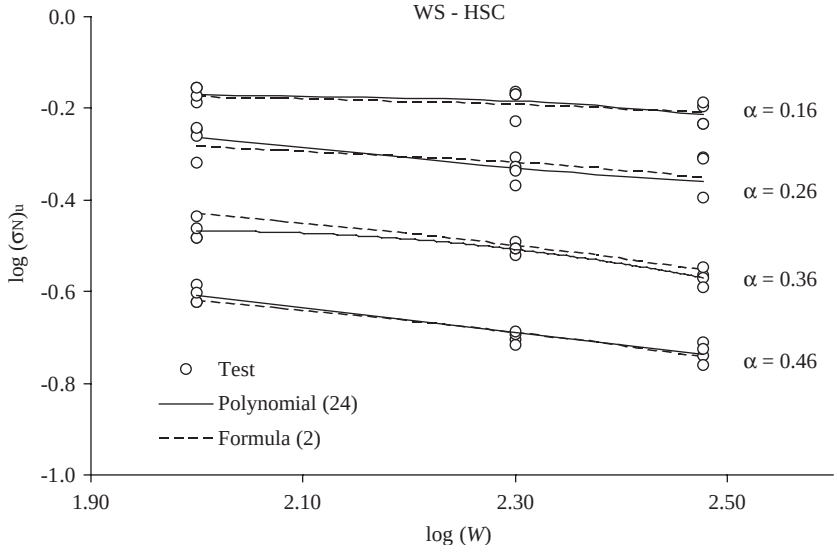

Fig. 10. The variation of the measured nominal strength with the characteristic dimension, W of the WS specimen for HSC compared with polynomial (24) and formula (2).

Table 4
Coefficients C_1, C_2 and C_3 in (24) for the three concrete mixes

Mix	f_c (MPa)	α	$C_1(\alpha)$	$C_2(\alpha)$	$C_3(\alpha)$
NC for TPB	55	0.05	0.250	−0.315	0.253
		0.10	0.219	−0.848	1.168
		0.30	0.138	−0.356	0.347
		0.50	0.078	−1.248	3.690
NC for WS	60	0.16	0.150	−0.807	1.471
		0.26	0.133	−0.695	1.297
		0.36	0.079	−0.490	0.964
		0.46	0.049	−0.100	0.113
HSC for WS	100	0.16	0.171	−0.013	0.010
		0.26	0.147	−0.158	0.124
		0.36	0.088	−0.035	0.011
		0.46	0.069	−0.100	0.080

Table 5
Material parameters G_f and c_f in (3) for the three concrete mixes

Mix	f_c (MPa)	α	A_2	B_2 (mm)	G_f (N/m)	c_f (mm)
NC for TPB	55	0.05	0.263	533.91	45.94	90.97
		0.10	0.200	655.94	58.08	74.77
		0.30	0.186	121.27	30.05	23.69
		0.50	0.068	660.39	67.57	104.05
NC for WS	60	0.16	0.100	415.38	47.58	125.15
		0.26	0.077	597.95	56.73	193.44
		0.36	0.054	573.96	42.51	136.11
		0.46	0.033	991.56	47.02	231.12
HSC for WS	100	0.16	0.176	1066.98	324.65	289.33
		0.26	0.144	459.08	132.24	103.96
		0.36	0.119	162.50	50.82	30.83
		0.46	0.077	161.60	35.39	30.13

polynomial (24) is also plotted on Figs. 8–10. Also plotted on Figs. 8–10 are the predictions of formula (2), in which the coefficients A_2 and B_2 have been determined by linear regression as explained above in Section 1.

Fig. 11 compares the predictions of the theoretical model based on the FCM described in Section 3 with the test results. For brevity, the comparison is presented only for the TPB geometry. However, similar results are obtained also for WS geometry. It will be seen that the theoretical predictions using the elastic and fracture properties of the TPB mixes given in Table 2 are in good agreement with the test results. The predictions of formula (2) are also very close to the test results (Figs. 8–10). This is not surprising given that the coefficients A_2 and B_2 were determined by fitting the very same test results. A test of the usefulness of formula (2) as a predictive tool must therefore be sought by alternative means. Here it is tested by exploiting the relation (3) between the coefficients A_2 and B_2 and the material properties G_f and c_f for a given specimen geometry, i.e. for a given $g(\alpha)$ and $g'(\alpha)$. It will be recalled that G_f and c_f are, respectively, the specific fracture energy and the size of the FPZ corresponding to a very large specimen (theoretically when $W\to\infty$) for which the linear elastic fracture mechanics is applicable in principle.

The G_f so obtained will be different from the G_F used above. In fact, it has been argued that G_f is approximately equal to 0.25 G_F (Bazant and Becq-Giraudon [33]) and that it is equal to the area under the initial part of the tension softening diagram. Of course, for G_f to be a material parameter it must not vary with shape and size of the test specimen. For the three test concrete mixes, G_f and c_f values obtained from the relations (3) are given in Table 5, from which it is clear that the G_f is not a material constant.

5. Discussion

It has been shown that when the crucial simplifying assumptions made in the derivation of formula (4) are removed, the predictions of the resulting formulation based on the FCM are in good agreement with the test results for notched TPB specimens (Fig. 11). (The same procedure can be followed for WS specimens. However, for brevity, calculations for WS specimens are not included here). This

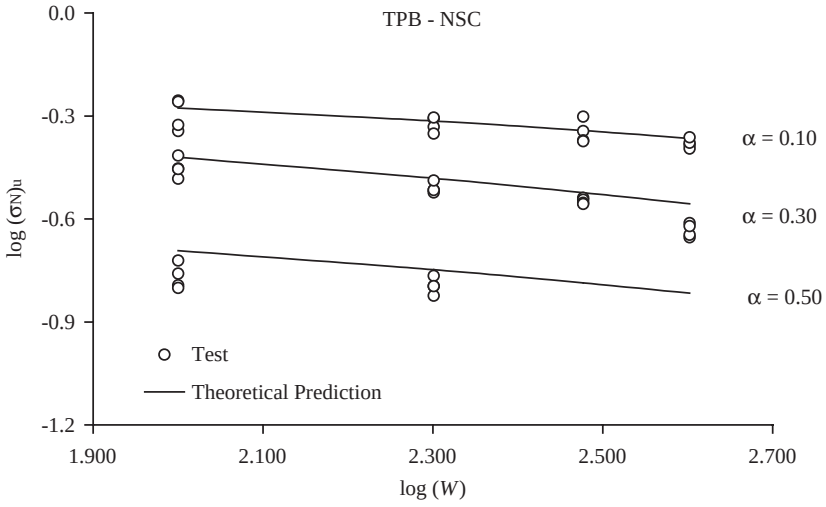

Fig. 11. The variation of the measured nominal strength with the characteristic dimension. W of the TPB specimen compared with the theoretical prediction.

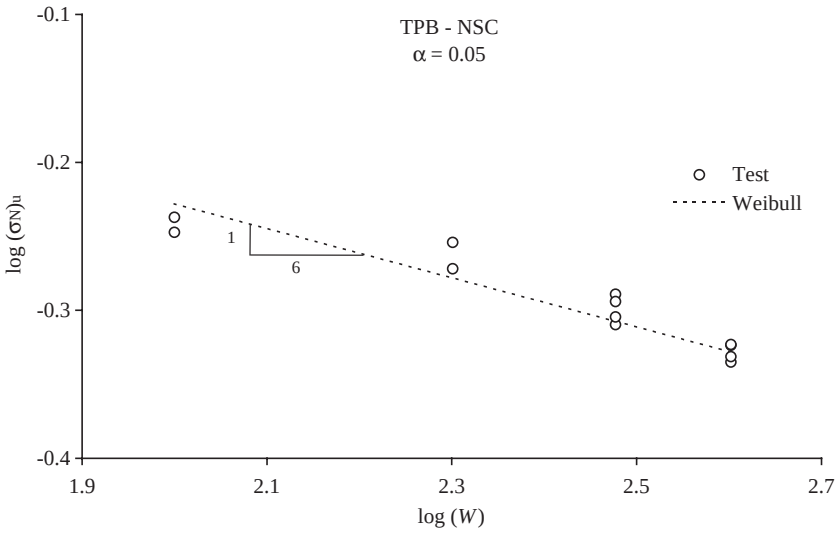

Fig. 12. The variation of the measured nominal strength of TPB specimen with a very small starter notch ($\alpha = 0.05$) with the specimen depth W compared with the Weinbull statistical size effect for concrete.

good agreement is a result of using G_F and $\sigma(w)$ in the FCM that are independent of the shape and size of the test specimen (Tables 1 and 2). The predictions of the size effect formula (2) are also in good agreement with the test results (Figs. 8–10). However, when the relationships (3) between the coefficients A_2 and B_2 appearing in this formula and the material properties G_f and c_f are exploited, the resulting material properties are found to vary significantly with the shape and size of the test specimen (Table 5). Thus this formula should not be used for predicting fracture properties of concrete mixes.

The test results for the nominal failure strength are faithfully represented by a third order polynomial in the characteristic size (formula (24)). The coefficients of this polynomial depend on α. It should be emphasized that the regression formula (24) is only applicable in the range of sizes of the test specimen, and it should not be used outside of this range.

Although both TPB and WS geometries belong to the so-called type 2 geometry ($g(\alpha)>0$, $g'(\alpha)>0$) (Bazant [11]), the observed strength size effect is somewhat different. Within the (small) range of sizes tested, formulas (2) and (24) are both in good agreement with the test data, despite the fact that the regression formula (24) predicts a positive curvature of the log $(\sigma_N)_u$ vs. log (W) plot for the NSC tested in WS geometry for small α and negative curvature for large α (=0.46) (Fig. 9), whereas formula (2) predicts a negative curvature for all α. The positive curvature for small α is predicted by the multi-scale fractal arguments forwarded by Carpinteri and his co-workers (see, e.g. Carpinteri [34]). Fig. 9 clearly shows the futility of using the curvature of the strength size effect curve constructed on the basis of a narrow range of specimen sizes that can be conveniently tested in a laboratory.

Finally, it is of some interest to study the weakening in the strength size effect as the size of the notch decreases

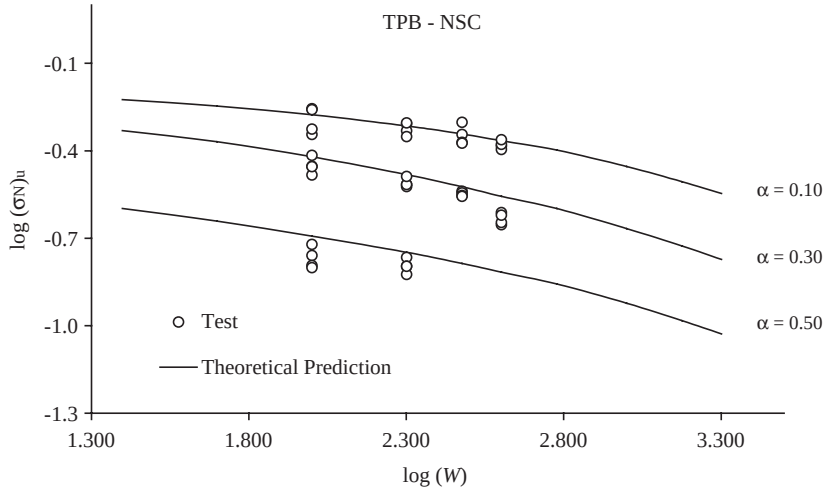

Fig. 13. The variation of the nominal strength with the characteristic dimension, W of the TPB geometry as predicted by the theoretical model in the extended size range from 25 to 2000 mm.

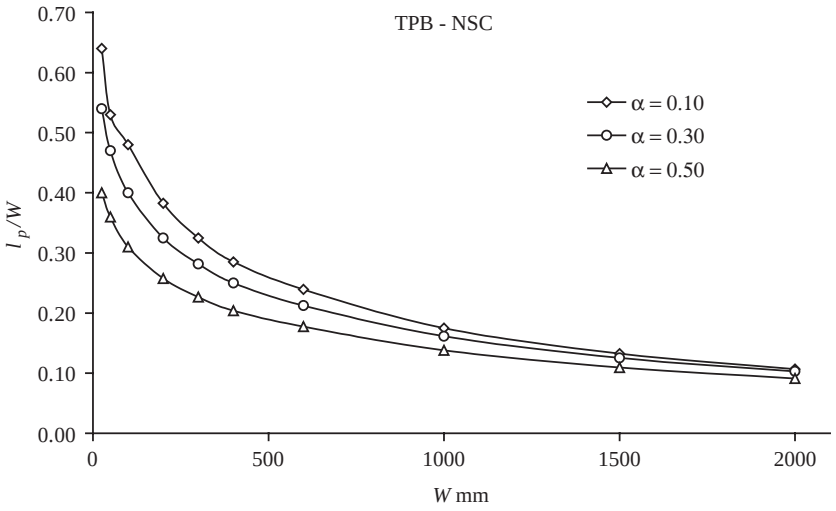

Fig. 14. The variation of the relative size of the FPZ with the characteristic dimension, W of the TPB geometry for the size range from 25 to 2000 mm.

with a view to judging whether or not there is a deterministic fracture mechanical size effect (over and above the statistical Weibull size effect) in un-notched quasi-brittle structures. For this the test results for the TPB specimens with a very small initial notch ($\alpha=0.05$) are again plotted in Fig. 12 on a log–log scale, together with the Weibull line which on the same scale has a slope close to $-1/6$ (Zech and Wittmann [35]). Note that it is not possible to test WS specimens with very small α (smaller than around $\alpha=0.15$) because they tend to fail prematurely at the re-entrant corners (Fig. 2). From Fig. 12 it is clear that there is a (small) size effect in the failure strength over and above the statistical Weibull size effect, but it is difficult to say with any degree of certainty as to whether this small difference is solely due to the deterministic fracture mechanical size effect. This is because casting and curing of concrete specimens induce their own size effects. Van Vliet and Van Mier [36] also noticed that uniaxial tension test strength data on un-notched specimens could be accurately described by Weibull statistics (apart from the very small test specimen) but cautioned against drawing any definitive conclusions on strength size effect from this fortuitous agreement because of the size effects induced by casting and curing of specimens.

In view of the fact that the theoretical model based on the FCM and the use of size-independent G_F and $\sigma(w)$ of a concrete mix is able to predict the strength size effect accurately in the range of sizes of TPB specimens tested in the laboratory, the model has been used to predict the nominal failure strength outside of this range. The size of notched TPB beams, made from the same NSC mix from which the test beams were made, was varied between $W=25$ mm and $W=2000$ mm keeping the span to depth ratio constant at 4. This gave a size range of 1 : 80. Three notch to depth ratios were considered, $\alpha=0.1$, 0.3 and 0.5. The results of this prediction are shown in Fig. 13, together with the test results. The relative size of the FPZ (l_p/W) is shown in Fig. 14 from which it is clear that l_p/W decreases significantly as W increases. For example, it drops from 0.64 to 0.107, as W increases from 25 to 2000 mm for $\alpha=0.10$. This confirms conclusively that nonlinear theory of fracture is essential for structures of small size but that large concrete structures with cracks can be analysed by linear elastic fracture theory.

6. Improved formula (4)

We have seen above that the theoretical model based on the FCM is able to predict accurately not only the test results in the narrow range of sizes tested in the laboratory but also outside of it (Fig. 13). However, these predictions are only available to those who can perform the computations. On the other hand, the regression polynomial (24) is restricted to the narrow size range of test specimens and thus not particularly helpful to a designer. For the above reasons, it would be most helpful to have the computational results available in a simple analytical form, as, e.g. formula (4) but without its drawbacks. This analytical

Table 6
Coefficients $D_1,\ldots,D_4$ in (25) and (28) for the three concrete mixes

Mix	f_c (MPa)	α	$D_1(\alpha)$	$D_2(\alpha)$	$D_4(\alpha)$	$D_3(\alpha)$ (Eq. (26))
NC for TPB	55	0.05	0.263	0.493	0.081	0.022
		0.10	0.211	0.481	0.001	0.0003
		0.30	0.156	0.254	0.029	0.009
		0.50	0.066	0.371	0.194	0.007
NC for WS	60	0.16	0.161	0.084	0.055	0.053
		0.26	0.177	0.013	0.088	0.054
		0.36	0.090	0.029	0.026	0.040
		0.46	0.051	0.407	0.079	0.005
HSC for WS	100	0.16	0.177	1.412	0.382	0.024
		0.26	0.158	0.401	0.109	0.021
		0.36	0.096	0.901	0.054	0.003
		0.46	0.104	0.064	0.024	0.020

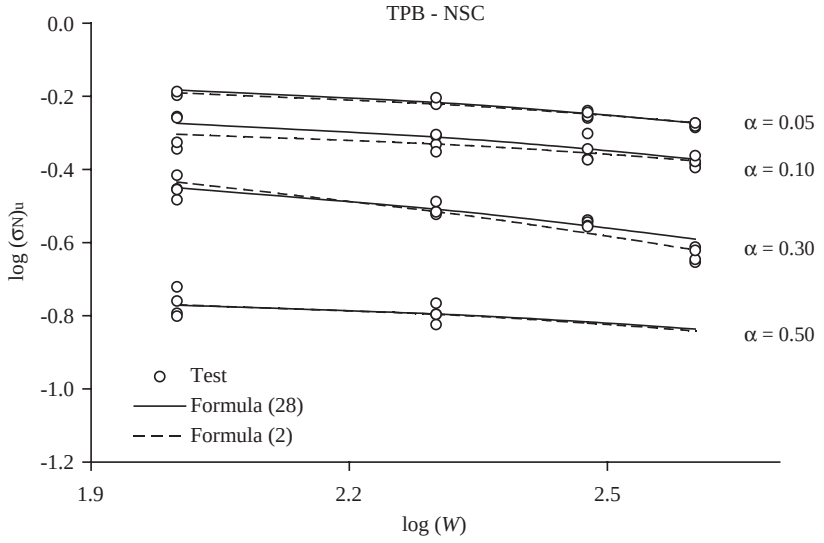

Fig. 15. The variation of the measured nominal strength with the characteristic dimension, W of the TPB specimen compared with formulae (28) and (2).

formula would replace the inadequate (4) and the regression polynomial (24).

With this aim in mind, we shall assume, based on the expected asymptotic behaviour that

$$(\sigma_N)_u^* = \frac{D_1}{\left(1+\frac{W^*}{D_2}\right)^{\frac{1}{2}}} + \frac{D_3}{\left(1+\frac{D_4}{W^*}\right)}, \tag{25}$$

where, $D_1,\ldots,D_4$ are coefficients to be determined by fitting the test results, and, for brevity, we have denoted $(\sigma_N)_u^* = (\sigma_N)_u / f_t$ and $W^* = W / l_{ch}$. In what follows, we shall however omit the asterisk sign.

The choice of (25) is dictated by the fact that the strength attains finite asymptotic values at both size extremes, i.e. when $W\to 0$ and $W\to\infty$. From (25) it is clear that $(\sigma_N)_u \to D_1$ as $W\to 0$ and $(\sigma_N)_u \to D_3$ as $W\to\infty$. It is also clear that $D_1 > D_3$. Moreover, (25) shows that $d(\sigma_N)_u/dW \to 0$ as $W\to\infty$. However, for $(\sigma_N)_u$ to tend to D_1 as $W\to 0$, we must have additionally that $d(\sigma_N)_u/dW \to 0$ as $W\to 0$. For this it is necessary and sufficient that

$$D_3 = \frac{D_1 D_4}{2D_2} \tag{26}$$

As $D_1 > D_3$, it follows from (26) that

$$\frac{D_4}{D_2} < 2 \tag{27}$$

Eq. (25) can therefore be rewritten as

$$\frac{(\sigma_N)_u}{f_t} = D_1(\alpha)\left(1+\frac{W/l_{ch}}{D_2(\alpha)}\right)^{-\frac{1}{2}} + \frac{D_1(\alpha)}{2D_2(\alpha)}\frac{W}{l_{ch}}\left(1+\frac{W/l_{ch}}{D_4(\alpha)}\right)^{-1}. \tag{28}$$

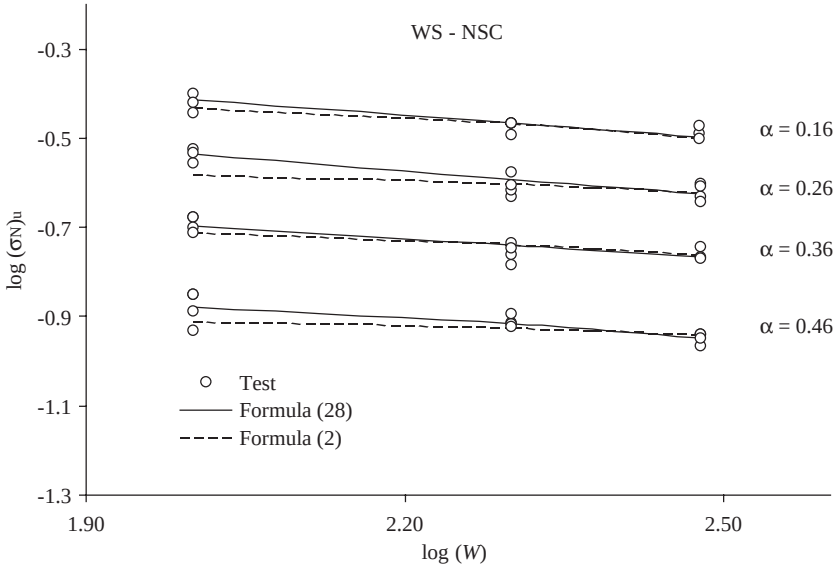

Fig. 16. The variation of the measured nominal strength with the characteristic dimension, W of the WS specimen for NSC compared with formulae (28) and (2).

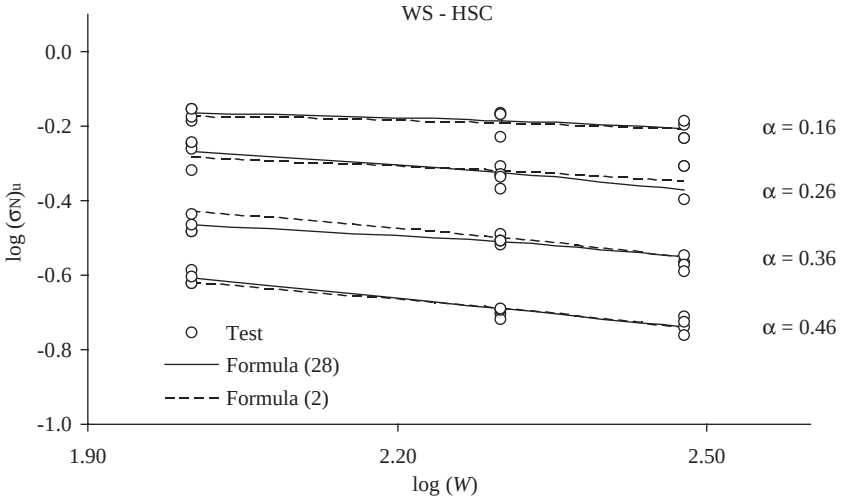

Fig. 17. The variation of the measured nominal strength with the characteristic dimension, W of the WS specimen for HSC compared with formulae (28) and (2).

Within the range of the sizes of specimens tested in the laboratory (28) also replaces the regression polynomial (24). The coefficients $D_1(\alpha)$, $D_2(\alpha)$ and $D_4(\alpha)$ are obtained by nonlinear regression of the test results and are given in Table 6, together with $D_3(\alpha)$ obtained using Eq. (26). Note that the inequality (27) is satisfied for all α and all three mixes.

The formula (28) is plotted on Figs. 15–17 for the three concrete mixes, together with formula (2). It will be seen that Eq. (28) fits the experimental data just as well as the regression polynomial (24).

Eq. (28) predicts a negative curvature for all three mixes over the range of sizes of the test specimens, just as formula (2) does.

Unlike the regression polynomial (24) which was based strictly on test data, Eq. (28) does have the correct asymptotic behaviour, although the coefficients $D_1(\alpha)$, $D_2(\alpha)$ and $D_4(\alpha)$ were determined from test data in a limited size range. In order to check whether or not it can be used outside of this narrow range, we shall compare its prediction with those of the theoretical/computational model (Fig. 13) for the NSC using TPB geometry for $\alpha = 0.10$, 0.30 and 0.50.

The comparison of predictions is shown in Fig. 18, from which it is clear that formula (28) can indeed be used in the size range 1 : 80 for shallow to moderate notches. The theoretical/computational predictions deviate from those of formula (28) for $\alpha = 0.50$. However, we believe that this is a result of the fact that the test results were only available for two depths for this ratio of notch to depth.

Formula (28) therefore replaces the inadequate formula (4), as well as the regression formula (24). The coefficients in this formula are established from specimens of a range of sizes and a range of notch to depth ratios that can be conveniently tested in a laboratory. The formula can then be used in a much larger size range (1 : 80) with confidence.

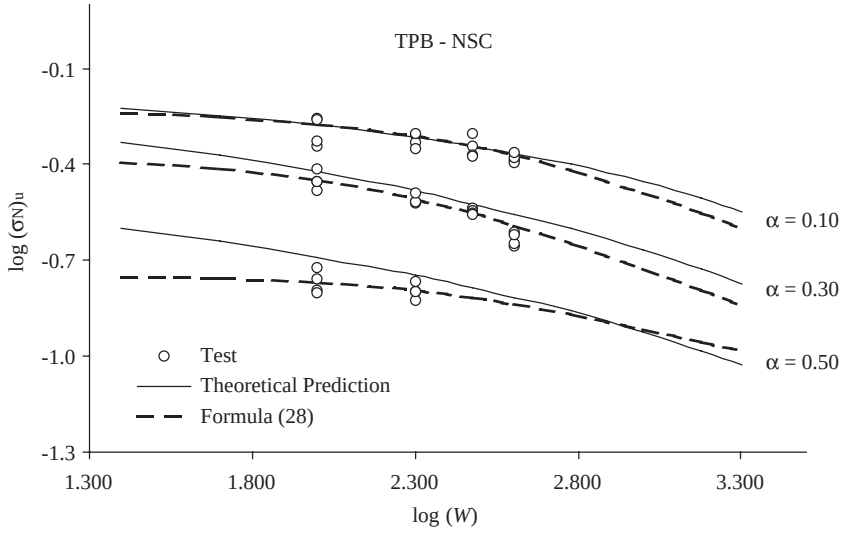

Fig. 18. Comparison of theoretical/computational predictions with those of formula (28) in the size range 1 : 8.

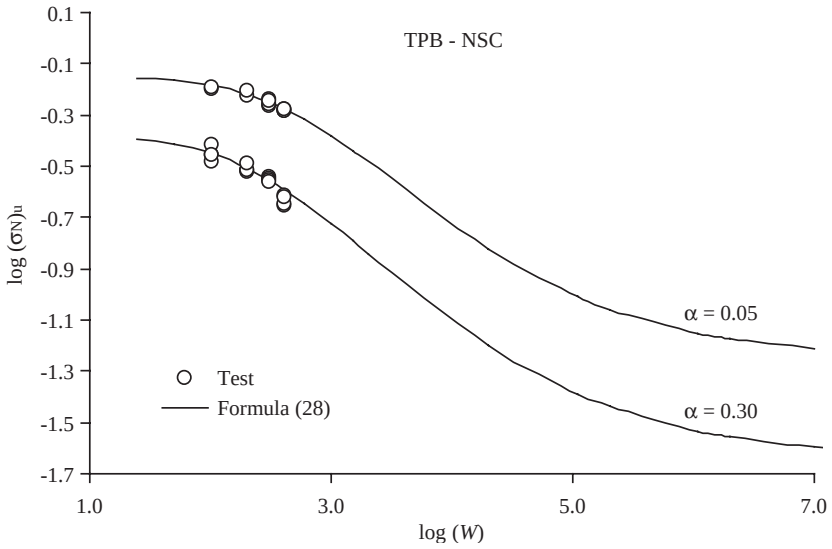

Fig. 19. Prediction of formula (28) over the size range $1:10^6$. The test data in the narrow size range are also shown ($\alpha = 0.05$ and 0.30).

As a matter of interest, we have plotted formula (28) in a still larger size range ($1:10^6$) in Figs. 19–21 of TPB and WS geometries for two notch to depth ratios, together with the test results. The formula seems to capture the whole range accurately.

7. Conclusions

Based on the work reported in this paper, the following conclusions can be drawn.

- A deterministic (as opposed to statistical) size effect exists in the strength of cracked concrete structures owing to the stress redistribution introduced by the presence of cracks manifested in the FPZ.
- The deterministic strength size effect becomes stronger as the size of the cracked structure increases but weakens as the size of the crack reduces relative to the size of the structure. These experimental observations are confirmed by theoretical/computational studies based on the FCM. For these studies it is important however to use the true, size-independent fracture energy and the corresponding tension softening diagram of the concrete mix that are independently measured.
- The theoretical/computational model that is in full agreement with the test results in the limited range of sizes tested in the laboratory can be extended beyond this range to include cracked concrete structures in the very large size range of $1:80$.
- The theoretical/computational results in this extended size range can be represented by a strength size effect formula that is very simple to use in practice and has the appropriate asymptotic behaviour at both size extremes.

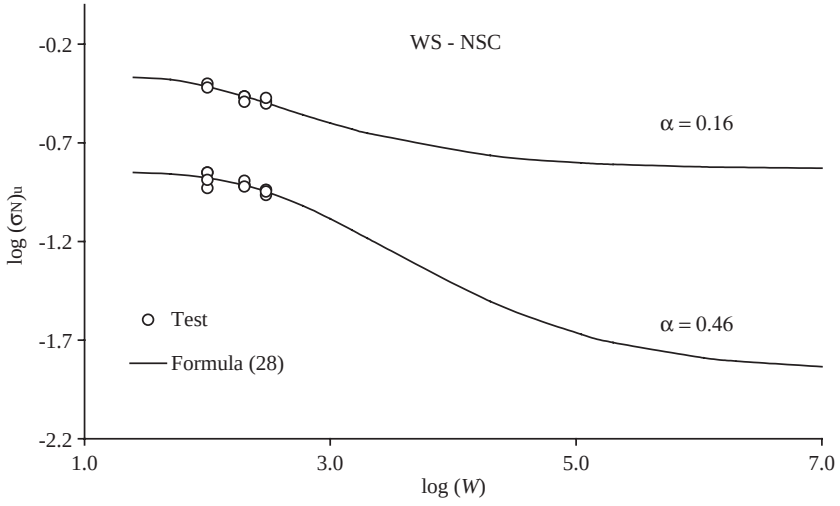

Fig. 20. Prediction of formula (28) over the size range $1:10^6$. The WS test data in the narrow size range are also shown ($\alpha = 0.16$ and 0.46).

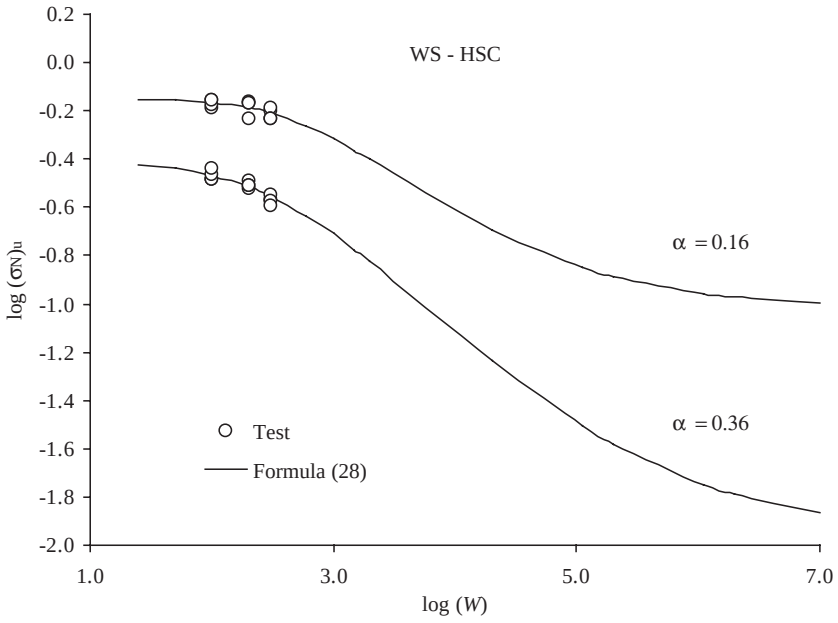

Fig. 21. Prediction of formula (28) over the size range $1:10^6$. The WS test data in the narrow size range are also shown ($\alpha=0.16$ and 0.36).

- Besides the mix properties (Young's modulus, E, direct tensile strength, f_t, and the true size-independent specific fracture energy, G_F) which must be independently measured, this simple formula contains three unknown coefficients which depend only on the size of the crack relative to the size of the structure (i.e. α).
- These three coefficients can be determined by regression on test results obtained on geometrically similar specimens of any shape but of varying sizes and α that can be conveniently handled in a laboratory. The formula can be used with confidence for cracked concrete structures in the range of at least $1:80$.

Acknowledgements

Financial support from UK EPSRC under grant number GR/R 11339 is gratefully acknowledged.

Appendix A

To solve the singular integral Eqs. (17) and (18), the FPZ is divided into $\boldsymbol{n}$ segments (from 1 to $\boldsymbol{n}$) with $(\boldsymbol{n}+1)$ nodes (from 0 to $\boldsymbol{n}$) as in Fig. A.1 below.

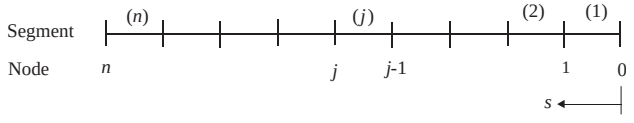

Fig. A.1. Division of FPZ into segments.

Node $\boldsymbol{j}$ is located at s_j—its distance from the tip of FPZ (Fig. A.1). Hence, $s_0=0$ and $s_n=l_p$. The cohesive stress at node $\boldsymbol{j}$ is σ_j; obviously $\sigma_0=f_t$.

In each segment ($\boldsymbol{j}$) with end points at $\boldsymbol{j}-1$ and $\boldsymbol{j}$, the distance from FPZ tip and the cohesive stress are interpolated linearly with their values at the end points:

$$s=\frac{1}{2}(1-x)s_{j-1}+\frac{1}{2}(1+x)s_j \tag{A.1}$$

$$\sigma=\frac{1}{2}(1-x)\sigma_{j-1}+\frac{1}{2}(1+x)\sigma_j. \tag{A.2}$$

The local coordinate $\boldsymbol{x}$ equals -1 at node $\boldsymbol{j}-1$ and 1 at node $\boldsymbol{j}$. For each node $\boldsymbol{i}$, $\boldsymbol{i}=1, 2,\ldots, \boldsymbol{n}$, $\boldsymbol{t_i}=\boldsymbol{s_i}$, the compatibility Eq. (17) can be written as

$$\int_0^{l_p} g(s,t_i)\left[\sigma(s)-\sigma_0\left(l_p-s\right)\right]ds=-w(t_i)$$
$$\text{or } \sum_{j=1}^{n}\int_{s_{j-1}}^{s_j} g(s,t_i)\left[\sigma(s)-\sigma_0\left(l_p-s\right)\right]ds=-w(t_i) \tag{A.3}$$

We write $\boldsymbol{\sigma_0(l_p-s)}$ as

$$\sigma_0\left(l_p-s\right)=\tilde{\sigma}_0\left(l_p-s\right)\cdot\sigma_r \tag{A.4}$$

where σ_r represents a reference stress.

According to the bilinear tension softening relationship (Fig. 3), $\boldsymbol{w(t_i)}$ can be represented through the cohesive stress as

$$w(t_i)=-\frac{\sigma_i}{a_k f_t}+\frac{b_k}{a_k} \tag{A.5}$$

where $\boldsymbol{b}_1=1$ and $\boldsymbol{k}=1$ or 2 depending on whether $\boldsymbol{w(t_i)}$ is less or greater than $\boldsymbol{w}_1$.

Substituting (A.2), (A.4) and (A.5 into (A.3) gives

$$\sum_{j=1}^{n}\int_{-1}^{1} g(s,t_i)\left[\frac{1}{2}(1-x)\sigma_{j-1}+\frac{1}{2}(1+x)\sigma_j-\tilde{\sigma}_0\left(l_p-s\right)\cdot\sigma_r\right] \times J\,dx-\frac{1}{\sigma_k f_t}\sigma_i=-\frac{b_k}{a_k}. \quad (A.6)$$

Here, it follows from (A.1) that

$$J=\frac{1}{2}\left(s_j-s_{j-1}\right). \quad (A.7)$$

Similarly, the smooth closure condition (18) can be written in a discrete form as

$$\sum_{j=1}^{n}\int_{-1}^{1} k(s)\left[\frac{1}{2}(1-x)\sigma_{j-1}+\frac{1}{2}(1-x)\sigma_j-\tilde{\sigma}_0\left(l_{\mathrm{p}}-s\right)\cdot\sigma_r\right] \times J\,dx=0. \quad (A.8)$$

Note that singular integrations need to be handled in (A.6) when $t_i=s_{j-1}$ or $t_i=s_j$ and $j=n$, and in (A.8) when $j=1$ (the segment includes the FPZ tip) and $j=n$. We have a total of $(n+1)$ equations (n from (A.6) and one from (A.8)) with $(n+1)$ unknowns, namely σ_1, σ_2,...,σ_n and σ_{r} ($\sigma_0=f_{\mathrm{t}}$).

If the maximum COD (at the bottom of a TPB specimen or at the bottom of the groove of a WS specimen) is less than w_1, the problem is still linear. If not, the problem is nonlinear. In this case, the solution is improved via iteration within each increment of FPZ. We choose a_k and b_k in (A.6) according to the results of the previous iteration. If the ratio of the increment of the maximum COD in the current iteration to the total increment is less than the required tolerance, i.e.

$$\left|\frac{g_{\max}\text{current iteration}-g_{\max}\text{previous }\textit{iteration}}{g_{\max}\text{current iteration}-g_{\max}\text{previous loading }\textit{step}}\right|<\textit{tol} \quad (A.9)$$

the solution is deemed to have converged. The iterations for the current loading step are stopped and the next increment of the FPZ (0.5 mm) made. In the computations, $tol=0.01$ was used. If the solution oscillates near the converged value, an average of the solutions of two successive iterations is used and the iterations continued until convergence. If the σ_{r} solution in the current increment of FPZ is smaller than in the previous one, it is clear that the peak the load-deformation curve has been passed. The analysis is then stopped.

References

[1] R.H. Leicester, The size effect of notches, Proc. 2nd Australian Conf. Mech. Mater. Struct., Melbourne, 1969, pp. 4.1–4.20.

[2] R.H. Leicester, Effect of size on the strength of structures, CSIRO Div. Build. Res. Paper, vol. 71, CSIRO, Melbourne, 1973, pp. 1–13.

[3] Z.P. Bazant, Size effect in blunt fracture: concrete, rock, metal, ASCE J. Eng. Mech. 110 (1984) 518–535.

[4] B.L. Karihaloo, Fracture Mechanics and Structural Concrete, Addison Wesley Longman, UK, 1995.

[5] Z.P. Bazant, Scaling of quasi-brittle fracture: asymptotic analysis, Int. J. Fract. 83 (1997) 19–40.

[6] Z.P. Bazant, E.P. Chen, Scaling of structural failure, Appl. Mech. Rev. 50 (1997) 593–627.

[7] A. Hillerborg, M. Modéer, P.E. Petersson, Analysis of crack formation and crack growth in concrete by means of fracture mechanics and finite elements, Cem. Concr. Res. 6 (1976) 773–782.

[8] B.L. Karihaloo, Size effect in shallow and deep notched quasi-brittle structures, Int. J. Fract. 95 (1999) 379–390.

[9] J. Planas, Z.P. Bazant, M. Jirasek, Reinterpretation of Karihaloo's size effect analysis for notched quasibrittle structures, Int. J. Fract. 111 (2001) 17–29.

[10] B.L. Karihaloo, H.M. Abdalla, Q.Z. Xiao, Size effect in concrete beams, Eng. Fract. Mech. 70 (2003) 979–993.

[11] Z.P. Bazant, Size effect in quasibrittle fracture: apercu of recent results, in: R. de Borst, J. Mazars, G. Pijaudier-Cabot, J.G.M. Van Mier (Eds.), Fract. Mech. Concr. Struct., vol. 2, Balkema, Lisse, The Netherlands, 2001, pp. 651–658.

[12] H.M. Abdalla, B.L. Karihaloo, Determination of size-independent specific fracture energy of concrete from three-point bend and wedge splitting tests, Mag. Concr. Res. 55 (2003) 133–141.

[13] X.Z. Hu, F.H. Wittmann, Fracture energy and fracture process zone, Mat. Struct. 25 (1992) 319–326.

[14] X.Z. Hu, F.H. Wittmann, Size effect on toughness induced by crack close to free surface, Eng. Fract. Mech. 65 (2000) 209–211.

[15] K. Duan, X.Z. Hu, F.H. Wittmann, Boundary effect on concrete fracture and non-constant fracture energy distribution, Eng. Fract. Mech. 70 (2003) 2257–2268.

[16] P. Nallathambi, B.L. Karihaloo, B.S. Heaton, Effect of specimen and crack size, water/cement ratio and coarse aggregate texture upon fracture toughness of concrete, Mag. Concr. Res. 36 (1984) 227–236.

[17] P. Nallathambi, B.L. Karihaloo, B.S. Heaton, Various size effects in fracture of concrete, Cem. Concr. Res. 15 (1985) 117–121.

[18] J. Planas, M. Elices, Conceptual and experimental problems in the determination of fracture energy of concrete, in: H. Mihashi, H. Takahashi, F.H. Wittmann (Eds.), Fracture Toughness and Fracture Energy Test Methods for Concrete and Rock, Balkema, Rotterdam, 1989, pp. 165–181.

[19] B.L. Karihaloo, H.M. Abdalla, T. Imjai, A simple method for determining the true specific fracture energy of concrete, Mag. Concr. Res. 55 (2003) 471–481.

[20] P.E. Roelfstra, F.H. Wittmann, Numerical method to link strain softening with failure of concrete, in: F.H. Wittmann (Ed.), Fracture Toughness and Fracture Energy of Concrete, Elsevier, Amsterdam, 1986, pp. 163–175.

[21] J.P. Ulfkjaer, S. Krenk, R. Brincker, Analytical model for fictitious crack propagation in concrete beams, ASCE J. Eng. Mech. 121 (1995) 7–15.

[22] J.F. Olesen, Fictitious crack propagation in fiber-reinforced concrete beams, ASCE J. Eng. Mech. 127 (2001) 272–280.

[23] G. Bolzon, R. Fedele, G. Maier, Parameter identification of a cohesive crack model by Kalman filter, Comput. Methods Appl. Mech. Eng. 191 (2002) 2847–2871.

[24] H.M. Abdalla, B.L. Karihaloo, A method for constructing the bilinear tension softening diagram of concrete corresponding to its true fracture energy, Mag. Concr. Res. 56 (2004) 597–604.

[25] B.L. Karihaloo, Q.Z. Xiao, Higher order terms of the crack tip asymptotic field for a notched three-point bend beam, Int. J. Fract. 112 (2001) 111–128.

[26] B.L. Karihaloo, H.M. Abdalla, Q.Z. Xiao, Coefficients of the crack tip asymptotic field for wedge-splitting specimens of different sizes, Eng. Fract. Mech. 70 (2003) 2407–2420.

[27] M. Elices, G.V. Guinea, J. Gómez, J. Planas, The cohesive zone model: advantages, limitations and challenges, Eng. Fract. Mech. 69 (2002) 137–163.

[28] F.J. Alaee, B.L. Karihaloo, A fracture model for flexural failure of beams retrofitted with CARDIFRC®, ASCE J. Eng. Mech. 129 (2003) 1028–1038.
[29] Q.Z. Xiao, B.L. Karihaloo, Approximate weight functions for singular and higher order terms of an edge crack in a finite plate, Eng. Fract. Mech. 69 (2002) 959–978.
[30] B.L. Karihaloo, Q.Z. Xiao, Accurate determination of the coefficients of elastic crack tip asymptotic field by a hybrid crack element with *p*-adaptivity, Eng. Fract. Mech. 68 (2001) 1609–1630.
[31] P.C. Paris, The Mechanics of Fracture Propagation and Solutions to Fracture Arrester Problems, Document D2-2195, The Boeing Company, 1957.
[32] H. Tada, P.C. Paris, G.R. Irwin, The Stress Analysis of Cracks Handbook, 2nd ed., Paris Productions, St. Louis, Missouri, 1985.
[33] Z.P. Bazant, E. Becq-Giraudon, Statistical prediction of fracture parameters of concrete and implications for choice of testing standard, Cem. Concr. Res. 32 (2002) 529–556.
[34] A. Carpinteri, Fractal nature of material microstructure and size effects on apparent mechanical properties, Mech. Mater. 18 (1994) 89–101.
[35] B. Zech, FH. Wittmann, A complex study on the reliability assessment of the containment of PWR: Part II. Probabilistic approach to describe the behaviour of materials, Nucl. Eng. Des. 48 (1978) 563–593.
[36] M.R.A. Van Vliet, J.G.M. Van Mier, Effect of strain gradients on the size effect of concrete in uniaxial tension, Int. J. Fract. 95 (1999) 195–219.
[37] A.M. Neville, Properties of Concrete, 3rd ed., Pitman, London, 1981.